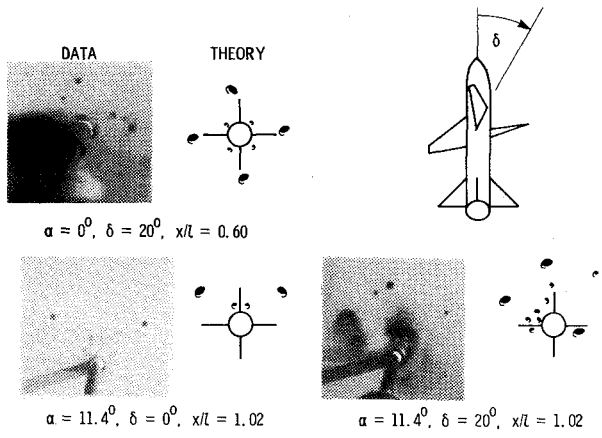

Fig. 3 Effect of forward fin deflection on vortex patterns: $\phi = 0$ deg.

At a roll angle of 22.5 deg, the top vertical fin is directly in the path of the right nose vortex. The rear fins have been removed from the missile in this photograph so as not to obstruct the view of the vorticity on the afterbody. This nose vortex appears in the data to have been displaced downward and to the right relative to the left nose vortex, and also appears weaker than the left vortex.

The corresponding theoretical calculations show that the observed movement of the right nose vortex is also predicted by the theory; however, no provision as yet exists in the theory to modify the strength of a vortex due to its interaction with a fin. There appears to be a fairly good agreement between the data and theory on the locations of the various vortices. The relative strengths also appear to agree, with the exception of the aforementioned right nose vortex.

At a roll angle of 45 deg, the nose vortices are no longer displaced and pass between the two upper fins. The theory plot reveals that all six of the primary vortices shown by the vapor screen photograph are predicted in approximately the same locations and relative strengths. The theory also predicts two additional vortices which are rather weak compared to the primary vortices. These weak vortices were predicted to originate on the inboard sections of the forward, upper fins as a result of the modified aerodynamic loading on these fins caused by the presence of the nose vortices. This weak vorticity does not appear in the experimental data as separate vortices.

Effect of Fin Deflection Angle

The computer codes developed in this study contain the capability to account for the effects of fin deflection on the computed vortex patterns. In order to investigate this aspect of the theory, vapor-screen photographs were obtained on the test missile in which all four of the forward fins were deflected 20 deg clockwise, as shown in the sketch contained in Fig. 3. The angle of roll is zero in this figure, and the fin deflection angles δ are 0 and 20 deg.

The data and theory in the upper left in this figure are for an angle of attack of zero and a fin deflection angle of 20 deg. The screen was located at 60% of the body length ($x/l = 0.60$). The data show that two vortices are created on each fin. One appears to be a normal outboard vortex, while the second is a weaker vortex which occurs on the inboard section of the fin, and is slightly counterclockwise relative to the outboard vortex.

The calculated vortices show exactly the same pattern as the data, except that the weaker vortices are somewhat more inboard and counterclockwise relative to the outboard vortices than they appear to be in the vapor-screen photographs. It should be noted that these vortices are caused entirely by the fin deflections since the angles of attack and roll are both zero. No vortices would be created, of course, if the fin deflection angle was zero.

The effects of fin deflection at an angle of attack of 11.4 deg are shown at the bottom of the figure, which contains results taken at the aft end of the missile. The deflected fins appear to create a rather complex pattern of vorticity in the vapor-screen photograph, including several discrete vortices and some areas of vorticity which are not rolled up into vortices. The computed results, which can only deal with discrete vortices, cannot duplicate these large areas of vorticity. In their place, however, the theory places a large number of individual vortices, as can be seen in the theory plot in the lower right part of Fig. 3.

Concluding Remarks

A theoretical and experimental effort has been made to develop a vortex-prediction capability on slender missiles at supersonic speeds. Using a slender fin-control missile as a test model, comparisons have been made between the calculated results and experimental data to assess the accuracy of the theory for various combinations on angle of attack, angle of roll, and fin deflection angle. The theory, based on a sparse number of discrete vortices, is capable of accurately predicting the number, location, and relative strengths of individual vortices which develop over the missile, but cannot predict vortex sheets or diffuse vorticity whenever they occur.

References

[1] Dillenius, M.F.E. and Nielsen, J.N., "Computer Programs for Calculating Pressure Distributions Including Vortex Effects on Supersonic Monoplane or Cruciform Wing-Body-Tail Combinations with Round or Elliptical Bodies," NASA CR 3122, April 1979.

A80-065

Differential Absorption Factors Between Two Area Elements in a Cylinder

90005

Masao Furukawa*
National Space Development Agency of Japan, Tokyo, Japan

Introduction

In connection with the thermal design of spacecraft, several computational procedures have been developed for dealing with radiant interchange between gray surfaces. One of them is the absorption factor method first introduced by Saunders[1] and then elaborated by Gebhart.[2-4] This method has not attracted as much notice as the radiosity approach which has been commonly used for temperature prediction. This is because, for many engineering purposes, the absorption factor concept is not as practical as the radiosity concept.

However, this method has a remarkable feature that absorption factors are independent of the temperatures of participating surfaces, whereas radiosities are dependent on them. Hence, for some configurations, the absorption factor method may greatly facilitate mathematical treatment of radiative heat transfer. Cylinders are of interest from this point of view. In addition, cylinders can be regarded as

Received June 11, 1979; revision received Feb. 15, 1980. Copyright © American Institute of Aeronautics and Astronautics, Inc., 1979. All rights reserved.

Index category: Radiation and Radiative Heat Transfer.

*Engineer, First Group of Satellite Design.

simplified models of space telescopes, tubular heat exchangers, gravity gradient rods, and so on. A finite-length cylinder or an infinitely long one are therefore chosen as the subject of this analysis.

Finite-Length Cylinder

The cylinder analyzed here is $2L$ in length and r in radius. The central axis is taken as the Z axis, and both open ends are specified as $Z=\pm L$. For simplicity, all length quantities are hereafter placed in the following dimensionless forms:

$$z=Z/r \qquad l=L/r \tag{1}$$

The inner surface is assumed to be a gray diffuse emitter which allows both diffuse and specular reflections in accordance with the relation $\epsilon+\rho_S+\rho_D=1$. The symbols ϵ, ρ_S, and ρ_D denote the emittance, the specular reflectance, and the diffuse reflectance, respectively.

Attention is first paid to two infinitesimal ring elements, dA and dA', at z and z' on the inside of the cylinder. The net heat transfer from dA to dA' can be expressed in terms of the differential absorption factor $B(z,z')$. This factor is defined here as the proportion of radiation emitted from dA which is eventually absorbed at dA'. The differential exchange factor $E(z,z')$ is then introduced for determining $B(z,z')$ in which we are now interested. The factor $E(z,z')$ shows a generalized view factor specifying the proportion of radiation leaving dA which arrives at dA' directly or after all possible intervening specular reflections.

The factor $B(z,z')$ consists of two portions. The first is the proportion of radiation emitted from z and absorbed at z', but considering only the radiation that goes directly from z to z' or that reaches z' after only specular reflections; the second is that involving indirect heat transfer due to diffuse reflections. The first portion is readily estimated as $\epsilon E(z,z')$. For a general ring element at ξ, $\rho_D E(z,\xi)$ represents the amount of radiation from z which is diffusely reflected at ξ around the interior after reaching ξ either directly or by only specular reflections. Only a part of this reflected radiation is absorbed at z'. This probability is given by $B(\xi,z')$ because any reflected radiation from ξ behaves in the same manner as the radiation directly emitted from ξ. The second portion is, therefore, obtained by integrating $\rho_D E(z,\xi)B(\xi,z')$ over all such elements $d\xi$. Thus, one has the following linear integral equation from which $B(z,z')$ can be derived:

$$B(z,z')=\epsilon E(z,z')+\rho_D\int_{-l}^{l}E(z,\xi)B(\xi,z')\,d\xi \tag{2}$$

The factor $E(z,z')$ is given by Perlmutter and Siegel,[5] but the infinite series in their expression is inconvenient for mathematical treatment. For this reason, the following approximation is employed:

$$E(z,z')\approx(\nu/2)e^{-\kappa|z-z'|} \tag{3}$$

where ν and κ are defined as

$$\nu=1+\frac{2}{3}\sum_{n=1}^{\infty}\frac{\rho_S^n}{n+2} \qquad \kappa=(1-\rho_S)\nu \tag{4}$$

The accuracy of Eq. (3) is discussed later with some numerical examples.

The advantage of this approximation is that the following formula involving a delta function is available:

$$\frac{d^2}{dZ^2}e^{-\kappa|z-z'|}-\kappa^2e^{-\kappa|z-z'|}=-2\kappa\delta(z-z') \tag{5}$$

Differentiating Eq. (2) twice with respect to z and applying Eq. (5), one has the following differential equation:

$$\frac{d^2}{dZ^2}B(z,z')-\mu^2B(z,z')=-\mu^2\delta(z-z') \tag{6}$$

where $\mu=\sqrt{\epsilon\nu\kappa}$. Since Eq. (5) holds also for μ, it is easily seen that Eq. (6) has a special solution of the form $e^{-\mu|z-z'|}$. Then, it is apparent that a general solution of Eq. (6) is written as $C(z')e^{\mu z}+D(z')e^{-\mu z}$. The unknown functions $C(z')$ and $D(z')$ are determined by substituting this expression into Eq. (2). The final result is arranged as

$$B(z,z')=\frac{\mu}{2}\left[\frac{2f}{1-f^2}\{f\cosh\mu(z-z')-\cosh\mu(z+z')\}+e^{-\mu|z-z'|}\right] \tag{7}$$

where f is given by

$$f=\frac{\kappa-\mu}{\kappa+\mu}e^{-2\mu l} \tag{8}$$

Now, attention is directed to the radiant interchange between a ring element at z and a circular opening at the left ($z=-l$) or right ($z=l$) end of the cylinder. The radiation exchange between them can be formulated in the same way, as previously mentioned. The differential exchange factor $E^*(z,\mp l)$ replaces $E(z,z')$. The superscript * discriminates $E^*(z,\mp l)$ from $E(z,\mp l)$, referring to the ring elements located at both ends. The factor $E^*(z,\mp l)$ is also given by Perlmutter and Siegel,[5] but for convenience one takes the following approximation:

$$E^*(z,\mp l)\approx(\nu^*/4)e^{-\kappa^*(l\pm z)} \tag{9}$$

where ν^* and κ^* are defined as

$$\nu^*=1+\frac{2}{3}\sum_{n=1}^{\infty}\frac{\rho_S^n}{(n+1)(n+2)} \qquad \kappa^*=(1-\rho_S)\nu^* \tag{10}$$

Since the differential absorption factor $B^*(z,\mp l)$ plays a role similar to $B(z,z')$, it is determined from the following integral equation corresponding to Eq. (2):

$$B^*(z,\mp l)=E^*(z,\mp l)+\rho_D\int_{-l}^{l}E(z,\xi)B^*(\xi,\mp l)\,d\xi \tag{11}$$

where both openings are treated as black surfaces. Equation (11) is transformed into the following differential equation by using Eq. (5):

$$\frac{d^2}{dZ^2}B^*(z,\mp l)-\mu^2B^*(z,\mp l)=(\kappa^{*2}-\kappa^2)E^*(z,\mp l) \tag{12}$$

The solution of Eq. (12) is expressed as

$$\begin{aligned}B^*(z,\mp l)=&\frac{\nu^*}{4}\frac{\kappa-\mu}{\kappa^{*2}-\mu^2}\frac{e^{-(\kappa^*+\mu)l}}{1-f^2}\\&\times\{(\kappa\mp\kappa^*)e^{\mp\kappa^*l}(e^{\mu z}-fe^{-\mu z})\\&+(\kappa\pm\kappa^*)e^{\pm\kappa^*l}(e^{-\mu z}-fe^{\mu z})\}+(\nu^*/4)f_0e^{\mp\kappa^*z}\end{aligned} \tag{13}$$

where f_0 is given by

$$f_0=\frac{\kappa^{*2}-\kappa^2}{\kappa^{*2}-\mu^2}e^{-\kappa^*l} \tag{14}$$

The radiative transfer from a circular opening at the end to a ring element in the interior of the cylinder is now con-

sidered. So far as the factor $E^*(\mp l,z)$ is concerned, it is evident that the reciprocity rule holds

$$E^*(\mp l,z)=E^*(z,\mp l) \tag{15}$$

However, such a rule does not hold with regard to $B^*(\mp l,z)$. The factor $B^*(\mp l,z)$ is computed from the following representation:

$$B^*(\mp l,z)=\epsilon E^*(\mp l,z)+\rho_D\int_{-l}^{l}E^*(\mp l,\xi)B(\xi,z)\,d\xi \tag{16}$$

Substituting Eqs. (7) and (9) into Eq. (16), one has the following expression different from Eq. (13):

$$B^*(\mp l,z)=\frac{\epsilon\nu^*}{4}f_0e^{\mp\kappa^*z}+\frac{\epsilon\nu^*}{8\mu}(f_{1,2}e^{-\mu z}+f_{2,1}e^{\mu z}) \tag{17}$$

where f_1 and f_2 are given by

$$f_{1,2}=(\kappa^2-\mu^2)e^{-\kappa^*l}\left\{\frac{2f^2}{1-f^2}\frac{\sinh(\mu\mp\kappa^*)l}{\mu\mp\kappa^*}-\frac{2f}{1-f^2}\frac{\sinh(\mu\pm\kappa^*)l}{\mu\pm\kappa^*}-\frac{e^{-(\mu\mp\kappa^*)l}}{\mu\mp\kappa^*}\right\} \tag{18}$$

Infinitely Long Cylinder

For an infinitely long cylinder, the internal radiation exchange is independent of axial coordinates. It is basically governed by the differential view factor $F(\varphi,\varphi')$ between two narrow longitudinal area elements dA and dA' at angular positions φ and φ'. The expression of $F(\varphi,\varphi')$, shown elsewhere,[6,7] is generalized so as to include contributions of specular reflections.

Because of the circular geometry, there are only two optical paths by which the radiation from dA can reach dA' after n specular reflections. One of them must pass the position located $1/(n+1)$ of the angular distance from φ to φ', while the other is required to pass the position located at its complimentary angular distance. The intensity of such radiation is, therefore, proportional to the sum of the view factor between two area elements separated by an angle $|\varphi-\varphi'|/(n+1)$ and that separated by an angle $(2\pi-|\varphi-\varphi'|)/(n+1)$. But, only a part of this amount, estimated at $\rho_S^n/(n+1)$, can reach dA' because of absorption and beam broadening. Thus, the expression defining the differential exchange factor is

$$E(\varphi,\varphi')=\frac{1}{4}\sin\frac{|\varphi-\varphi'|}{2}+\frac{1}{4}\sum_{n=1}^{\infty}\frac{\rho_S^n}{n+1}\left\{\sin\frac{|\varphi-\varphi'|}{2(n+1)}+\sin\frac{2\pi-|\varphi-\varphi'|}{2(n+1)}\right\} \tag{19}$$

The differential absorption factor $B(\varphi,\varphi')$ can now be derived from the following integral equation similar to Eq. (2):

$$B(\varphi,\varphi')=\epsilon E(\varphi,\varphi')+\rho_D\int_0^{2\pi}E(\varphi,\psi)B(\psi,\varphi')\,d\psi \tag{20}$$

Although it is generally very difficult to solve Eq. (20) because of the multiplicity of its kernel, there exists a special case where an exact solution can be found. If $\rho_S=0$, then Eq. (20) reduces to an integral equation of the Fredholm type in which the kernel is simply expressed as $\frac{1}{4}\sin|\varphi-\varphi'|/2$. In this special case, Eq. (20) is transformed into a differential equation by the use of the following formula:

$$\frac{d^2}{d\varphi^2}\sin\mu|\varphi-\varphi'|+\mu^2\sin\mu|\varphi-\varphi'|=2\mu\delta(\varphi-\varphi') \tag{21}$$

The resulting differential equation is written as

$$\frac{d^2}{d\varphi^2}B(\varphi,\varphi')+\mu^2B(\varphi,\varphi')=\mu^2\delta(\varphi-\varphi') \tag{22}$$

where $\mu=\sqrt{\epsilon}/2$. From Eqs. (21) and (22), it is seen that Eq. (22) has a special solution of the form $\sin\mu|\varphi-\varphi'|$. General solutions are then written as $C(\varphi')\cos\mu\varphi+D(\varphi')\sin\mu\varphi$. The unknown functions $C(\varphi')$ and $D(\varphi')$ are determined by substituting this expression into Eq. (20) with $\rho_S=0$. The final result is arranged as

$$B(\varphi,\varphi')=(\mu/2)\{\cos\mu(\varphi-\varphi')\cot\pi\mu+\sin\mu|\varphi-\varphi'|\} \tag{23}$$

It is now desirable to find a more general expression than Eq. (23) and $\mu=\sqrt{\epsilon}/2$, because they are inapplicable to such cases as $\rho_S\neq0$. However, for any generalized expressions, such periodicity as $B(\varphi+2\pi,\varphi')=B(\varphi,\varphi')$ should be satisfied because of the circular geometry. This implies that the form of Eq. (23) will still hold without any significant changes. An easier generalization of Eq. (23) is, therefore, made by modifying μ only. Equation (23) associated with the expression

$$\mu=\sqrt{\epsilon\nu\kappa}/2 \tag{24}$$

provides a rough approximation of the solution of Eq. (20). In Eq. (24), κ is given by the same expression as Eq. (4), but ν is defined as

$$\nu=1+2\sum_{n=1}^{\infty}\frac{\rho_S^n}{n+1}\sin\frac{\pi}{n+1} \tag{25}$$

Numerical Results and Discussions

A finite-length cylinder with uniform wall heat generation is presented for discussion. Assuming that there is no radiation from the circular openings and no wall heat conduction, the following integral equation governs the wall temperatures:

$$\epsilon\theta^4=1+\epsilon\int_{-l}^{l}\theta^4(\xi)B(\xi,z)\,d\xi \tag{26}$$

The symbol θ shows the dimensionless temperature defined as

$$\theta^4=\sigma T^4/q_w \tag{27}$$

where σ, T, and q_w denote the Stefan-Boltzmann constant, the absolute temperature, and the heat added per unit wall area, respectively. Differentiating Eq. (26) twice with respect to z and applying Eq. (6) , an easily solved second-order differential equation is obtained. The solution is written as

$$\theta^4=(c-\mu^2z^2)/2\epsilon \tag{28}$$

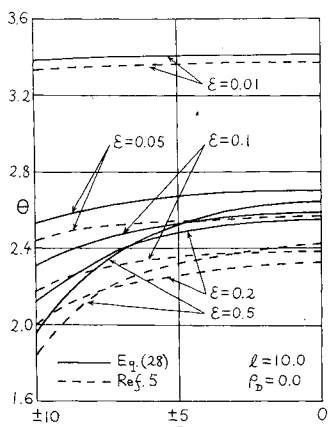

Fig. 1 Dimensionless wall temperature distributions.

where c is given by

$$c=\left[\frac{2f}{1+f}\left\{(\mu^2l^2+2)\sinh\mu l-2\mu l\cosh\mu l\right\}+(\mu^2l^2+2\mu l+2)e^{-\mu l}\right]\times\left(\frac{2f}{1+f}\sinh\mu l+e^{-\mu l}\right)^{-1} \quad (29)$$

Since the use of Eq. (3) causes some errors in the analysis involving specular reflections, the accuracy of Eq. (7) must be evaluated for practical applications. Comparison between results computed from Eq. (28) and those given in the literature[5] provide numerical justification of Eq. (3). The computation is performed for purely specular surfaces specified as $\rho_D=0.0$. Numerical results for a cylinder with $l=10.0$ are shown in Fig. 1. This figure displays dimensionless wall temperature distributions for various emittances. For two curves specified by the same emittance value, the difference is fairly small. Furthermore, they are alike in tendency although the curve based on Eq. (28) is slightly higher than the reference curve[5] drawn in dashes. From such good agreement, it is concluded that Eq. (7) can be used as a basis of thermal analyses relating to cylindrical configurations.

References

[1] Saunders, O.A., "Notes on Some Radiation Heat Transfer Formulae," *Proceedings of the Physical Society, (London)*, Vol. 41, 1928-29, pp. 569-575.

[2] Gebhart, B., "Unified Treatment for Thermal Radiation Transfer Processes-Gray, Diffuse Radiators and Absorbers," ASME Paper 57-A-34, 1957.

[3] Gebhart, B., "A New Method for Calculating Radiant Exchanges," *ASHAE Journal, Heating, Piping, Air Conditioning*, July 1958, pp. 131-135.

[4] Gebhart, B., "Surface Temperature Calculations in Radiant Surroundings of Arbitrary Complexity for Gray, Diffuse Radiation," *International Journal of Heat Mass Transfer*, Vol. 3, 1961, pp. 341-346.

[5] Perlmutter, M. and Siegel, R., "Effect of Specularly Reflecting Gray Surface on Thermal Radiation through a Tube and from its Heated Wall," *Transactions of the ASME, Journal of Heat Transfer*, Vol. 85, Feb. 1963, pp. 55-62.

[6] Graham, J.D., "Radiation Heat Transfer around the Interior of a Long Cylinder," *Journal of Spacecraft and Rockets*, Vol. 7, March 1970, p. 372-374.

[7] Sparrow, E.M. and Cess, R.D., *Radiation Heat Transfer*, Brooks Cole Pub. Co., 1967, p. 110.

A80-066 40009 40010 60009

Dual-Fuel Propulsion: Recent Results for Earth-to-Orbit Vehicles

James A. Martin* and Alan W. Wilhite†
NASA Langley Research Center, Hampton, Va.

Introduction

IN the first two decades of space flight, the most important goals of vehicle design were to establish the feasibility and capability for flight beyond the atmosphere. Multiple expendable stages were appropriate for these pioneering flights. The Space Shuttle,[1] which will begin orbital flights soon, will be the first step toward a more mature transportation system with low operational cost and the capability to accomplish a broad range of mission requirements.

When the Space Shuttle concept was selected, traffic projections did not justify designs that were more desirable operationally. The development cost would have been too high with the available technology.[2] The situation will be different, however, in the near future for follow-on transportation systems. The improved transportation offered by the Space Shuttle will spur traffic growth. In fact, user demand through 1982 may already be more than the Space Shuttle can accommodate.[3] Proposed space activities could potentially increase traffic greatly.[4] Improved technology will also be available for new transportation systems. Many technology improvements have already been developed by the Space Shuttle program. Others are being developed by the air transport industry, the military, and others. Still further technology improvements are now foreseen but will require development by an advanced vehicle program.[5,6]

One of the promising technologies for advanced vehicles is dual-fuel propulsion. Salkeld first showed the advantage that can be achieved by using two fuels in a single-vehicle stage if a high-density-impulse fuel is used first and a high-specific-impulse fuel is used second.[7] Martin then showed that this approach might not be attractive for Earth-to-orbit vehicles if separate engines are used in series, but that it might be attractive if a single engine could use both fuels in series.[8] Martin also showed that separate engines could be attractive if they operate in parallel initially. Figure 1 is a schematic diagram of these concepts. Beichel then proposed a dual-expander engine which uses two fuels in parallel initially to maximize benefits of dual-fuel propulsion for advanced Earth-to-orbit transportation systems.

The purpose of this note is to provide an update of dual-fuel propulsion efforts. Engine options are discussed and some Earth-to-orbit vehicle results are updated.

Engine Options

Several engine options have been studied for dual-fuel propulsion in Earth-to-orbit vehicles.[12-16] The best performance and cost results[10,11] have been achieved with the dual-expander engine[9] which utilizes a coannular nozzle. The simplest engine combination for dual-fuel vehicles, from a technology development point of view, uses the Space Shuttle main engine (SSME) in parallel with a hydrocarbon engine that has hydrogen cooling and a hydrogen-rich gas generator. This engine has been called the hydrogen gas generator (HGG) engine. The dual expander and HGG engines have in

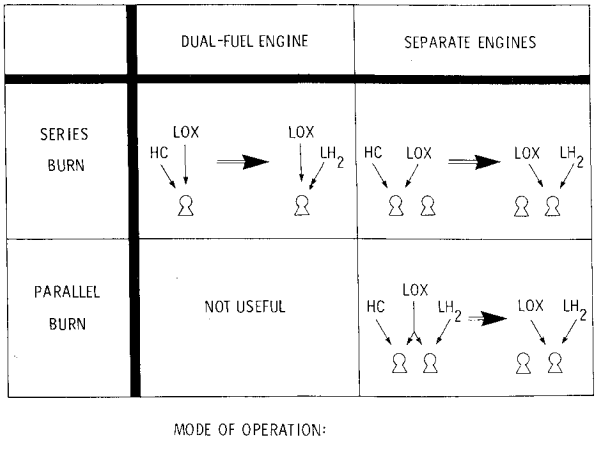

Fig. 1 Schematic diagram of engine concepts.

Presented as Paper 79-0878 at the AIAA/NASA Conference on Advanced Technology for Future Space Systems, Hampton, Va., May 8-11, 1979; submitted June 18, 1979; revision received Feb. 28, 1980. This paper is declared a work of the U.S. Government and therefore is in the public domain.

Index categories: LV/M Propulsion and Propellant Systems; LV/M Mission Studies and Economics; Liquid Rocket Engines and Missile Systems.

*Aerospace Engineer, Space Systems Division. Member AIAA.

†Aerospace Engineer, Space Systems Division.